ADVANCED
FUNCTIONAL
MATERIALS

Laser-Induced Secondary Crystallization of CsPbBr₃ Perovskite Film for Robust and Low Threshold Amplified Spontaneous Emission

Yueqing Shi, Ruxue Li, Guoxin Yin, Xuanyu Zhang, Xuanchi Yu, Bingheng Meng, Zhipeng Wei,* and Rui Chen*

All-inorganic perovskite nanocrystals (NCs) have received extensive attention for next-generation thin film devices due to their excellent optical properties, such as strong light absorption, high carrier mobility, and defect tolerance. However, significant challenges remain to obtain high-quality perovskite thin films. Herein, a simple but effective post-treatment by laser irradiation for CsPbBr₃ NCs thin films is reported. Laser-induced secondary crystallization is observed in CsPbBr₃ NCs thin films after treatment. In addition, amplified spontaneous emission (ASE) with a low threshold (5.6 μJ cm⁻²) and a high gain value (743 cm⁻¹) is achieved. Based on optical measurements, it is attributed to the low defect density, reduced Auger recombination, and weak exciton–phonon interactions, which greatly suppress the nonradiative recombination channels. The ASE from the film after treatment has a high characteristic temperature (134 K), showing a stable optical gain performance that maintains its intensity for 35 h at room temperature (and 12 h at 40 °C). Finally, the proof-of-concept demonstration of graphic coding is shown. This study deepens the understanding of the optical gain mechanism of CsPbBr₃ perovskite films and provides a simple and convenient laser treatment that enables the fabrication of high-quality CsPbBr₃ perovskite thin films.

1. Introduction

Perovskite optoelectronic devices have attracted extensive research attention due to their numerous advantages such as high carrier mobility,[1] high optical absorption ability,[2] and good defect tolerance,[3] etc. Single crystal perovskites are good candidate to significantly reduce the density of trap states, leading to higher charge carrier mobility and longer diffusion length for advanced device performance. However, the development of single crystal perovskite based optoelectronic devices suffers from difficulties in material fabrication. Therefore, related research has turned to more easily synthesized perovskite nanocrystals (NCs),[4] which have broad application prospects in solution processing fabrication and flexible optoelectronic device applications. Significant progresses in perovskite NCs have been achieved during the past few years not only in highly efficient solar cells[5] and multicolor light-emitting diodes (LEDs),[6] but also in low threshold optically pumped lasers.[7]

Materials with high crystal quality are the basis of excellent devices. However, perovskite NCs thin film encounter problems in this regard. On one hand, undesirable pinholes in the thin film reduce the effective area of the device.[8] On the other hand, inherent structural defects such as grain boundaries will cause ion migration and moisture exposure, which results in environmental instability and degrade the device performance.[9] To reduce the detrimental effects of morphology and defect, post-treatments have always been applied to perovskite thin film for improved quality and performance,[10] such as hot plate annealing,[11,12] solvent annealing,[13,14] vacuum-assisted annealing,[15,16] and so on. Among them, hot plate annealing has been widely recognized as a simple and inexpensive method for perovskites. However, the disadvantage of hot plate annealing is that the electrodes and other layers of the devices will be affected by high temperatures. In comparison, the crystalline and morphology of perovskite film can be essentially improved by both solvent annealing and vacuum-assisted annealing. For

Y. Shi, R. Li, X. Zhang, X. Yu, B. Meng, R. Chen
Department of Electrical and Electronic Engineering
Southern University of Science and Technology
Shenzhen 518055, P. R. China
E-mail: chenr@sustech.edu.cn

R. Li, B. Meng
School of Microelectronics and Materials Engineering
Guangxi University of Science and Technology
Liuzhou, Guangxi 545006, P. R. China

R. Li, B. Meng, Z. Wei
State Key Laboratory of High Power Semiconductor Laser
School of Physics
Changchun University of Science and Technology
Changchun, Jilin 130022, P. R. China
E-mail: weizp@cust.edu.cn

G. Yin
Department of Materials Science and Engineering
Southern University of Science and Technology
Shenzhen, Guangdong 518055, P. R. China

The ORCID identification number(s) for the author(s) of this article can be found under https://doi.org/10.1002/adfm.202207206.

**ADVANCED
SCIENCE NEWS**
www.advancedsciencenews.com

**ADVANCED
FUNCTIONAL
MATERIALS**
www.afm-journal.de

the solvent annealing, the surface and grain boundary of perovskite films are eroded by polar solvents vapor to further promote secondary crystallization.[13,14] Vacuum-assisted annealing can passivate pinholes formation in the films by rapid evaporation of the remaining components in the perovskite precursor.[15,16] Nonetheless, both of the methods need to be performed in the glove box with a special atmosphere. Therefore, the perovskite annealing process is still in the early stage of rapid and large-scale fabrication, which begs for more desirable novel treatments.

Recently, we have encapsulated perovskite microcrystal by a dense Al_2O_3 layer,[17] which forms a vacuum-like growth chamber. Self-structural healing of perovskite has been observed under high temperature or prolonged laser irradiation, thereby enhancing the optical and thermal stability of perovskites. However, complete capsulation of perovskite will limit electrical injection for industrial applications. Significant progress in secondary grain growth has been reported by modifying perovskite surfaces with organic ammonium. It was found that the high surface energy anisotropy induced by organic ammonium is the driving force of secondary grain growth.[18] The internal property evolution of the whole perovskite thin film is caused by surface modification. However, such surface modification must be carried out at high temperature with the help of organic ammonium.

In this work, the secondary crystallization of $CsPbBr_3$ NCs thin film is driven directly by laser irradiation in ambient atmosphere, which significantly improves the optical gain properties and stability of the samples. X-ray diffraction (XRD) and in situ photoluminescence (PL) measurements indicate that the perovskite NCs thin film has a larger grain size and better crystal quality after laser irradiation. Green amplified spontaneous emission (ASE) was obtained from the samples at room temperature with a low threshold and a high net modal gain. The power and temperature dependent PL measurements and the transient absorption (TA) measurements show that laser treatment reduces defect density, slows Auger recombination, and suppresses electron–phonon interaction. Thus, the greatly reduced nonradiative recombination pathway enables low threshold ASE of laser-treated films. The physical mechanism of ASE in laser-treated films has been discussed, which is considered to be a gain phenomenon due to inelastic exciton–exciton scattering. Furthermore, the modified film exhibits excellent ASE stability under continuous excitation with a characteristic temperature of 134 K. These results suggest that the laser-induced secondary crystallization strategy can lead to stable and low threshold optical gain medium by reducing nonradiative recombination. This method could pave the way for post-treatment of perovskite film with arbitrary shape or large scale by controlling the laser beam.

2. Results and Discussion

The $CsPbBr_3$ NCs were synthesized and purified as described in the experimental section. **Figure 1**a shows the normalized UV-Vis absorption and the PL spectra of the $CsPbBr_3$ NCs. The absorption band edge of $CsPbBr_3$ NCs is located at 502 nm, while the emission is centered at 515 nm. The inset of Figure 1a presents the transmission electron microscope (TEM) image of the NCs, which shows that the NCs maintain a cubic shape with an average length of 10 ± 1 nm. The NCs solution was drop-casted onto a quartz substrate to prepare the $CsPbBr_3$ NCs thin film. Immediately, the film was exposed to a pulse
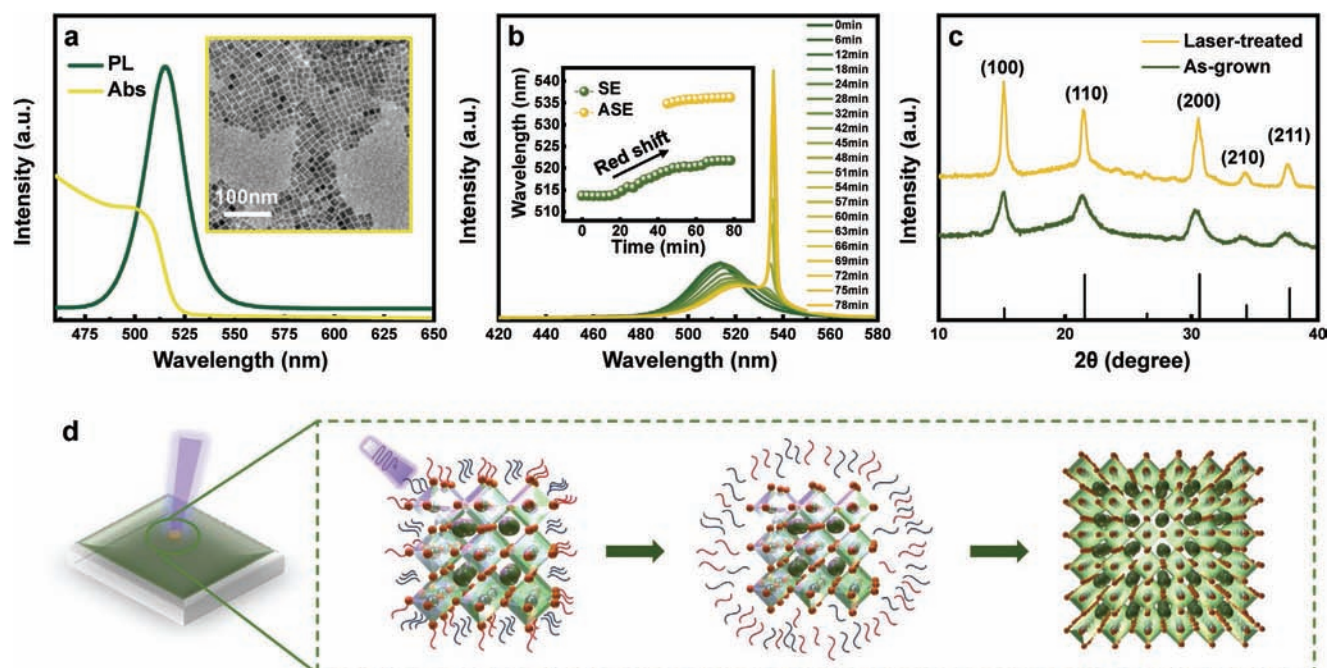

Figure 1. Static spectra and structural characterizations. a) PL and absorption of the as-grown $CsPbBr_3$ perovskite NCs thin film. The inset is the TEM image of the samples. b) The in situ emission monitoring of the sample under excitation as a function of time. The inset shows the corresponding peak position of the spontaneous emission and ASE. c) XRD patterns of the samples before and after laser irradiation. d) Schematic diagram for the laser-induced secondary crystallization.

laser operating at 355 nm (pulse width of 1 ns and repetition rate of 20 Hz) with an excitation density around 1.4 mJ cm^{-2}. In situ PL monitoring during the laser irradiation is plotted in Figure 1b, where the inset illustrates the peak wavelength as a function of time. In the picture, it can be seen that during the first 20 mins of laser irradiation, only a broad spontaneous emission (SE) peak appears in the PL spectrum, and its intensity decreases while the peak position maintains at 514 nm. From 20 to 50 mins, the SE intensity decreases with the redshift of the peak. After 50 mins, a narrow ASE peak appears with a rapid increase of intensity as a function of time. Initially, the decrease of SE intensity may be attributed to the defects generated by the photo-desorption of the surface ligands. The TEM image provides some evidence for ligand removal as shown in Figure S1 (Supporting Information), where a shape transition from nanocube to nanosphere is observed during laser irradiation. This shape transition may lead to the removal of surface ligands due to the lower surface energy of the nanosphere.[19] The Fourier transform infrared (FTIR) data in Figure S2 (Supporting Information) shows that the relative intensity of the characteristic peaks significantly decreases after laser treatment, which implies the removal of the ligands. The redshift of the SE indicates that the laser-induced secondary crystallization leads to an increase of grain size. As shown in Figure 1c, the XRD patterns of the as-grown and laser-treated CsPbBr$_3$ thin film have the same peak positions, corresponding to the cubic phase structure of CsPbBr$_3$ (PDF#540 752).[20] This indicates that the crystal structure is preserved after laser irradiation. In addition, the increased intensity and narrowing shape of the diffraction peaks indicate improved crystallinity and larger grain size. All of the above observations reveal the laser-induced secondary crystallization of CsPbBr$_3$ NCs thin film. A schematic diagram of this process is illustrated in Figure 1d. There are two steps during the laser irradiation process, namely, ligand removal and secondary crystallization. In the first step, ligands are removed from the surface of CsPbBr$_3$ NCs by absorbing photon energy from the irradiated laser. In the next step, the NCs contact each other through surface bonds. The ion migrations are induced by laser irradiation, which leads to secondary crystallization and finally a thinner and denser film as shown in Figure S3 (Supporting Information). It has been reported that the driving force for secondary grain growth in perovskite with organic ammonium is the anisotropic surface energy of crystal planes.[18] In some studies, laser irradiation is reported to cause selective removal of ligands from specific crystal surfaces, increasing the surface energy.[21] Therefore, it is believed that the driving force of the secondary crystallization observed herein may be provided by the laser-induced surface energy anisotropy.[22] To explore the role of moisture and oxygen in the secondary crytallization, controlled experiments under atmosphere and nitrogen (N$_2$) were performed, respectively. As shown in Figure S4 (Supporting Information), narrow ASE appears after laser treatment for both cases. With identical experimental conditions, the ASE was observed after 63 mins of laser irradiation for the film under atmosphere. However, it takes 90 mins for the case of N$_2$. This implies that moisture and oxygen play an auxiliary role for secondary crystallization. It is reported that the moisture absorbed within grain boundaries creeps and merges adjacent grains for longer ion diffusion length.[23] Moreover, oxygen can reduce the defects at the crystal interface and inside, corrode the unstable nanocrystal to release dissociated ions which migrate to the large crystals and contribute to the crystal growth.[24] Therefore, it is expected that the secondary crystallization will be promoted with further careful control of environmental conditions. It is worth mentioning that similar results can be obtained using continuous wave laser, nanosecond laser, and femtosecond laser, as shown in Figure S5 (Supporting Information). For ultrafast femtosecond laser pulses, the thermal effect is negligible.[25] Simulation of temperature distribution under laser irradiation as a function of depth and the irradiation time were performed. For the femtosecond pulse laser irradiation, the maximum temperature is 24 °C at 500 fs as shown in Figure S6 (Supporting Information). Therefore, it can be concluded that thermal effect is not the cause of the secondary crystallization.[26]

To characterize the optical gain of the thin film, a femtosecond pulsed laser (355 nm, 1 kHz, 100 fs) was used. **Figure 2**a shows the power-dependent PL spectra of the perovskite thin film after laser irradiation. Broad SE dominates when the excitation density is below the threshold (P_{th}) around 5.6 µJ cm^{-2}. With a further increase in excitation density, a redshifted ASE (centered at ≈535 nm) with a full width half maximum (FWHM) of ≈4 nm appears. The corresponding integrated intensity and FWHM as a function of excitation density are shown in Figure 2b, which confirms the transition from SE to ASE. The net optical modal gain (g) is then determined by the variable
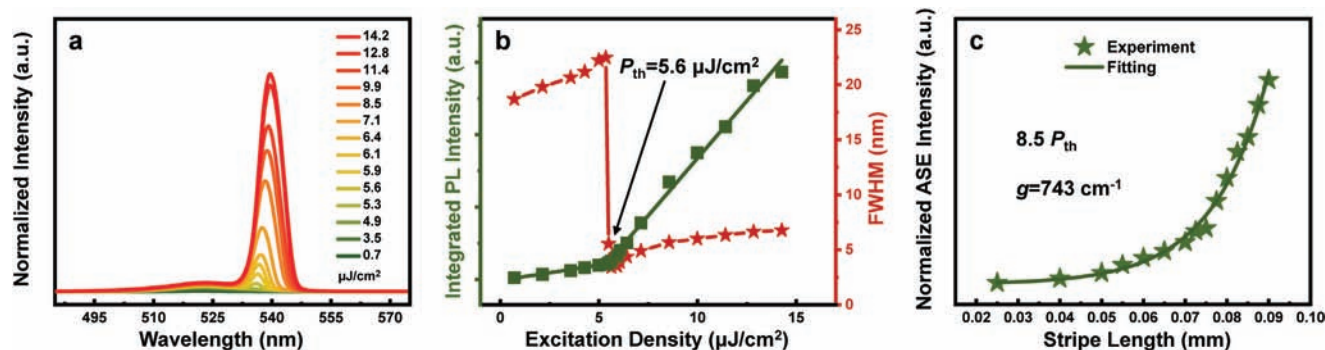

Figure 2. Optical gain measurements. a) The ASE from the laser-treated film under different excitation densities. b) The change of integrated intensity (green) and FWHM (red) as a function of excitation density. c) ASE intensity of the laser-treated film as a function of stripe length.

ADVANCED
SCIENCE NEWS
www.advancedsciencenews.com

ADVANCED
FUNCTIONAL
MATERIALS
www.afm-journal.de

stripe length (VSL) approach. The gain coefficient of 743 cm^{-1} under excitation density around 8.5 P_{th} is derived from the best fit to the data in Figure 2c. It is noted that the optical gain of the laser-treated thin film is among the best of CsPbBr$_3$ materials.[27]

It is well-known that nonradiative recombination channels including trap states, Auger recombination and phonon scattering widely hinder the optical gain of the materials. Therefore, comparative analysis of the carrier dynamics between the as-grown and laser-treated films had been performed to discuss the generation of gain in the laser-treated perovskite NCs thin film.

Defects are generally considered as a fast nonradiative pathway to compete with radiation recombination.[28] The dynamics of photo-generated charge carrier density (n_c) can be described with the following set of differential equations,

$$\frac{dn_c(t)}{dt} = -\sum_i a_i n_c(t) n_{TP}^i(t) - \frac{n_c(t)}{\tau_0}$$
$$\frac{dn_{TP}^i(t)}{dt} = -a_i n_c(t) n_{TP}^i(t) \tag{1}$$

where $n_{TP}^i(t)$ is the density of trap states. a_i is the coefficient which represents the ability of the trap states to capture carriers. Thus, the relationship between the integrated PL intensity (I_{PL}) and the initial photo-generated charge carrier density $n_c(0)$ can be expressed as,

$$n_c(0) = n_{TP}(0)\left(1 - e^{-\frac{a\tau_0 I_{PL}}{k}}\right) + \frac{I_{PL}}{k} \tag{2}$$

where τ_0 is the lifetime of carriers under low excitation density, k is a constant. $n_c(0)$ can be determined by the carrier density which can be found in Supporting Information. As shown in **Figure 3**a and Figure S7 (Supporting Information), fitting the experimental data by Equation (2) yields a defect density of around 4.9×10^{17} cm^{-3} for the laser-treated sample. In contrast, the defect density in the as-grown sample is determined to be around 3.4×10^{18} cm^{-3}, which is about one order of magnitude higher than the laser-treated samples. It indicates that the laser-induced secondary crystallization reduces the surface-to-volume ratio and the formation of defects, which results in better crystal quality of the samples.

Population inversion can be achieved under high excitation density. However, a fast multi-exciton Auger recombination process will occur simultaneously. The Auger recombination lifetime of perovskite is ≈10–100 ps,[29] which is significantly faster than the radiative recombination, resulting in a rapid decrease of optical gain, especially in material systems with large overlap of electron and hole wavefunctions.[30] To further discuss the effect of laser treatment on the Auger recombination, TA measurements at different excitation densities were performed (Figure S8, Supporting Information). The as-grown and laser-treated samples were pumped by a femtosecond laser with a pulse width of 100 fs at 355 nm. As shown in Figure 3b, under excitation density around 3.5 μJ cm^{-2}, the photo bleaching (PB) signal shows a relatively fast decay component. Considering that the threshold of ASE is above this excitation density and the lifetime of bound exciton recombination is
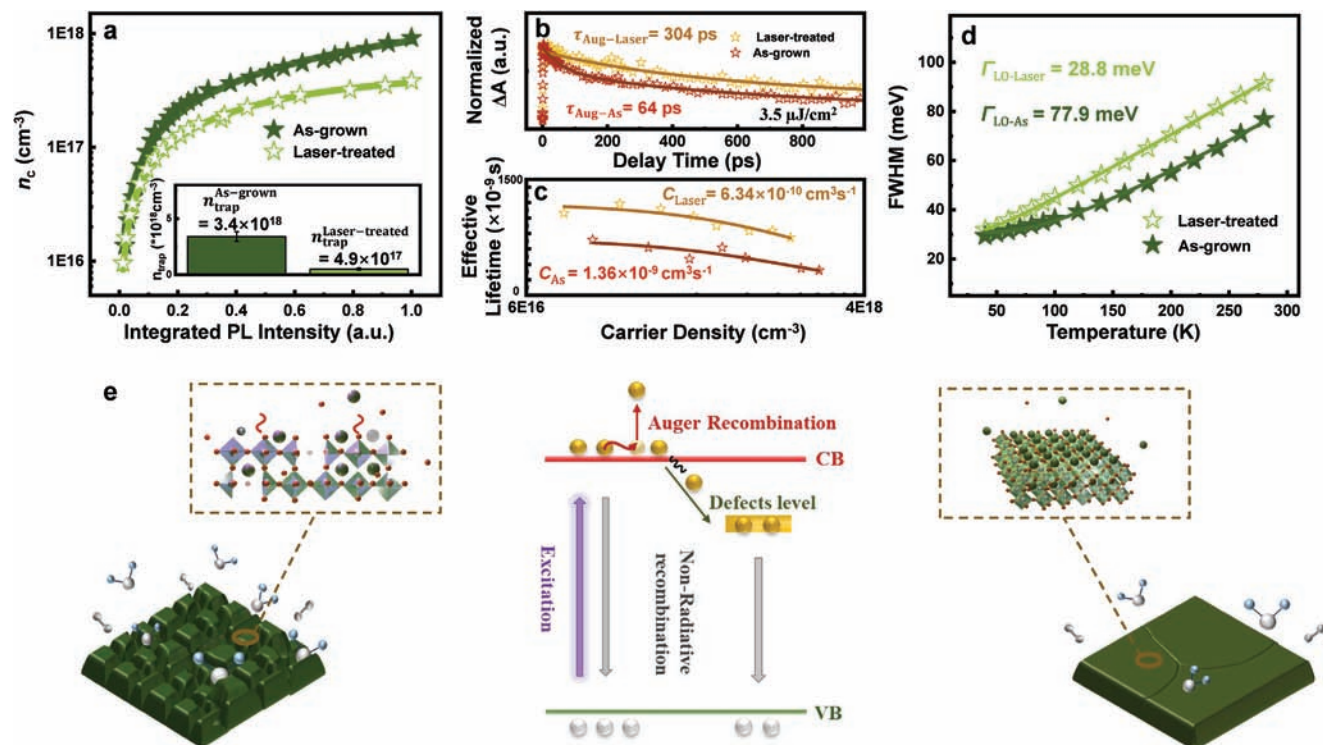

Figure 3. Nonradiative recombination channels of the as-grown and laser-treated films. a) Integrated PL intensity as a function of photon-generated exciton density within the low excitation range. b) PB kinetics of the as-grown and laser-treated films at 3.5 μJ cm^{-2}. c) The effective PL lifetime of the as-grown and laser-treated films as a function of carrier density. d) Emission FWHM versus temperature for the films. e) The schematic diagram of the nonradiative recombination channels.

**ADVANCED
SCIENCE NEWS**
www.advancedsciencenews.com

**ADVANCED
FUNCTIONAL
MATERIALS**
www.afm-journal.de

longer than 1 ns,[31] the fast decay component can be assigned to Auger recombination. From the fitting, the Auger lifetime of the perovskite NCs thin film increases from 64 to 304 ps after laser irradiation. The effective PL lifetime τ_{eff} was obtained as a function of the carrier density.[32] As shown in Figure 3c, the Auger recombination coefficient can be obtained from τ_{eff} as a function of the carrier density according to $\tau_{eff} = \frac{1}{B+CN/2}$, where B is the exciton recombination coefficient, C is the Auger recombination coefficient, and N is the initial photogenerated carrier density.[33] It can be seen from the fitting results that the Auger recombination coefficient C for the as-grown sample is 1.36×10^{-9} cm^3 s^{-1}, which is larger than that of the laser-treated film (6.34×10^{-10} cm^3 s^{-1}). This is consistent with the higher ASE threshold of the as-grown sample. The reduced Auger recombination process is due to the low carrier density caused by the larger grain size after laser irradiation.[34]

The interaction between exciton with lattice vibrations (phonons) via Coulombic interaction also results in a loss of excitons, which affects the optical gain of the materials.[35] Due to the different scattering mechanisms between carriers and phonons or impurities, the PL linewidth increases with temperature (Figure S9, Supporting Information), and the temperature-dependent FWHM of the emission can be expressed as,

$$\Gamma = \Gamma_{inh} + \gamma_{LA}T + \frac{\Gamma_{LO}}{\exp\left(\frac{E_{LO}}{k_BT}\right)-1} \quad (3)$$

where Γ_{inh} describes inhomogeneous broadening, γ_{LA} is the coupling strength between exciton and longitudinal acoustic (LA) phonon, Γ_{LO} is the coupling strength between exciton and longitudinal optical (LO) phonon, and E_{LO} is the LO phonon energy. In CsPbBr$_3$ perovskite materials, the LO phonons dominate the interaction,[36,37] and the contribution of LA phonons is negligible. The fit of $\Gamma = \Gamma_{inh} + \frac{\Gamma_{LO}}{\exp\left(\frac{E_{LO}}{k_BT}\right)-1}$ to the PL linewidth is plotted in Figure 3d, and the extracted E_{LO} of the as-grown and laser-treated samples are about 24.08 and 9.18 meV, respectively, which match with the reported values.[38,39] Moreover, the extracted Γ_{LO} of the as-grown sample is 77.9 meV, which is larger than the value of the laser-treated sample (28.8 meV). The increase of Γ_{LO} represents a higher energy loss due to stronger lattice vibration in the as-grown films. For the laser-treated films, the increased crystal stiffness caused by the larger grain size and better crystal quality may lead to the suppression of exciton–phonon coupling strength.[40]

It should be emphasized that the three processes mentioned above are not independent of each other, and they have a synergistic effect on nonradiative recombination. The nonradiative Auger recombination results in carrier Auger re-heating, and this excess energy has been shown to rapidly thermalize with the LO phonons, thereby accelerating nonradiative decay through electron–LO phonon interactions.[41] Moreover, electron–phonon interactions also play an important role in facilitating the transition of electrons from band edges to trap states.[42] In turn, trap states have been found to enhance the strength of the Fröhlich interaction in CsPbBr$_3$ perovskite NCs[43] and contribute to Auger recombination.[44] As can be seen from the discussion, the simultaneous presence of these three processes in the laser-treated samples significantly suppresses the nonradiative recombination, as indicated in Figure 3e, which is crucial for increasing optical gain and lowering the ASE threshold.

The original gain mechanism of ASE in the laser-treated CsPbBr$_3$ NCs thin film is also elucidated. Stimulated processes usually begin with intermediate excitation density where excitons can be treated as quasiparticles. During this process, exciton–exciton scattering and biexciton are formed due to collision. If the sample is excited more intensively, beyond the density known as the Mott density, the excitons typically transit to a metal-like electron hole plasma (EHP) state. All of these processes can lead to the emergence of new emissions and ultimately optical gain.

Due to the strong Coulomb interactions among multi-excitons in perovskite NCs, the biexciton mechanism has been reported as the gain mechanism in many recent reports.[45] The energy separation between exciton emission peak and ASE peak herein is estimated to be at least 58 meV, which greatly exceeds the biexciton binding energy reported in most perovskite nanocrystals.[46] It is shown that the biexciton binding energy decreases with the increase of perovskite size.[30] Therefore, the biexciton binding energy of the perovskite films with larger grain size after laser irradiation should be smaller,[47] and the experimental observations can help rule out that the optical gain is induced by biexcitons.

The possible origin related to EHP has also been investigated. According to literature,[48] within the EHP lasing region, the system loses its excitonic resonance properties and leads to bandgap renormalization. Therefore, the horizontal cut at the zero crossing of the transient reflect spectra should be redshifted. Moreover, the transient reflectance signal will no longer be antisymmetric at 50 fs, which is characteristic of EHP state. In our experiment, Figure S10 (Supporting Information) shows the TA spectra at $\Delta t = 100$ fs from the low density to the high density over the ASE threshold, both the zero-crossing point position and the anti-symmetric peak shape have not changed. Therefore, the EHP model can be ruled out based on the TA spectra features of our sample.

The exciton–exciton inelastic scattering process could also induce ASE. Power-dependent and temperature-dependent PL characterizations have been employed to investigate the exciton–exciton inelastic scattering. For the power-dependent PL, there is a clear redshift of the peak position with the increase of excitation density. While for the temperature-dependent PL, the peak position blueshifts first and then redshifts with the increase of temperature. Both of these phenomena can be explained by the exciton–exciton inelastic scattering. Schematic illustration of the inelastic interaction is shown in the inset of **Figure 4**c. Inelastic interactions occur between two excitons at $n = 1$. One of them is scattered onto the photon-like branch of the polariton curve, while the other is scattered to high excitonic energy level ($n > 1$). The exciton scattered into the polariton curve results in P-band emission with a smaller photon energy compare to 1st exciton (E_{ex}). The general form of the nth P-band emission can be expressed as,[49]

$$P_n = E_{ex} - E_b\left(1 - \frac{1}{n^2}\right) - 3\delta k_B T_{eff}, n = 2,3,4\cdots \quad (4)$$
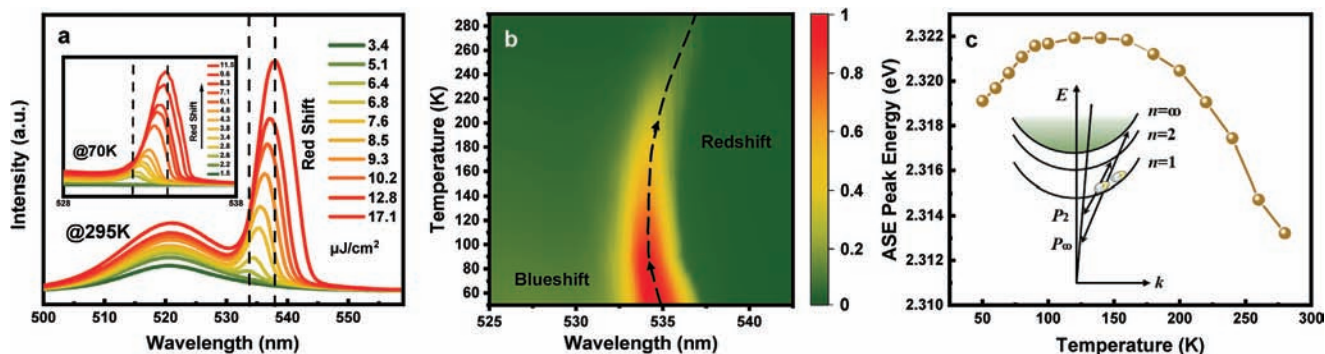
Figure 4. The original gain mechanism of ASE in the laser-treated film. a) The power-dependent emission spectra for various excitation intensities under 295 and 70 K (insert). b) 2D pseudocolor plot of the temperature-dependent PL spectra of the laser-treated film. c) Temperature dependence of stimulated emission peak energy fixed at 11.5 μJ cm^{-2}.

E_{ex} is the energy of free exciton, E_b denotes the exciton binding energy, n stand for the nth exciton level, δ is a constant ($0 < \delta < 1$) and k_B is the Boltzmann constant, T_{eff} is the effective temperature of excitonic system.

$$P_2 = E_{ex} - E_b\left(1 - \frac{1}{2^2}\right) - 3\delta k_B T_{eff} \tag{5}$$

$$P_\infty = E_{ex} - E_b - 3\delta k_B T_{eff} \tag{6}$$

$$P_2 - P_\infty = \frac{1}{4}E_b + 3\delta k_B \Delta T_{eff} \tag{7}$$

With the increase of exciton density, the excitons can be excited to lower energy level at polariton curve ($n = 2,3,4...$), so the value of term $E_b\left(1 - \frac{1}{n^2}\right)$ in Equation (4) increases. Moreover, the serious thermal effect of the excitation laser will lead to an increase of effective temperature (T_{eff}). As a result, the ASE redshifts as described in Equation (4). The redshift of ASE with excitation density has been observed at 295 and 70 K in our experiments as shown in Figure 4a. In Figure 4b,c, a clear blueshift and then redshift of peak position with temperature can be seen. During the temperature range, the excitation density is fixed at 11.5 μJ cm^{-2}, and the ASE can be approximately described by the P_∞ equation. As shown in Equation (6), the shift of ASE is the result of the competition between the increase of E_{ex} and the decrease of $-3\delta k_B T_{eff}$ terms. From 50 to 120 K, the ASE peak position shows a blueshift which is consistent with the previous report, where the blueshift of E_{ex} in CsPbBr$_3$ perovskite with temperature is due to the lattice thermal expansion effect.[50] When $T > 120$ K, an extraordinary opposite redshift is observed with the increase of temperature due to the increase of T_{eff}. All these ASE behaviors are highly accordant with exciton–exciton inelastic scattering.

Figure 5a,b show the ASE thresholds for the laser-treated thin film as a function of temperature and the long-time stability of ASE at room temperature and 40 °C (inset). As shown
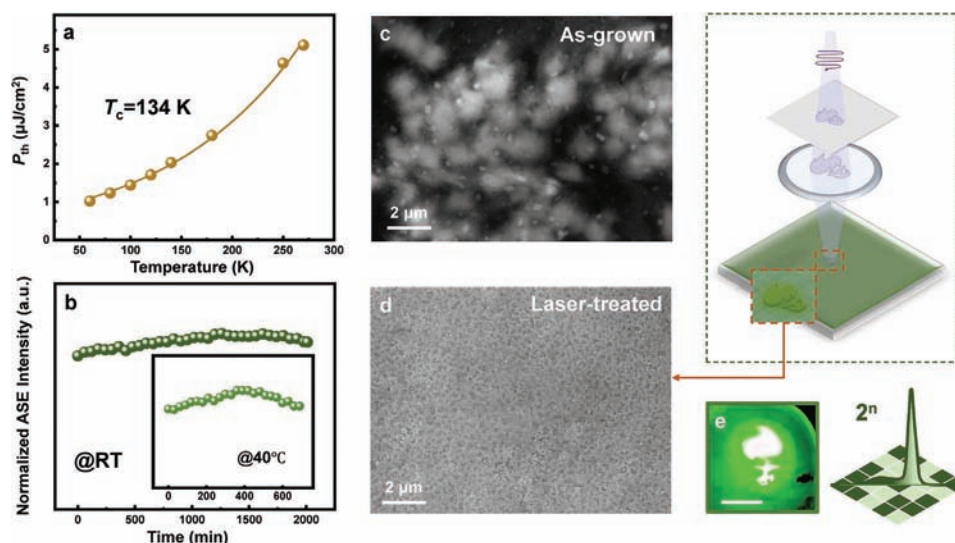

Figure 5. The optical gain stability measurements and optical graphic coding application. a) ASE thresholds for the laser-treated thin film as a function of temperature. b) The long-time stability measurement of ASE intensity at room temperature and 40 °C (inset). SEM images of c) the as-grown film and d) the laser-treated film. e) Photograph of the patterned CsPbBr$_3$ thin film under laser excitation. The scale bars are 3 mm.

**ADVANCED
SCIENCE NEWS**

www.advancedsciencenews.com

**ADVANCED
FUNCTIONAL
MATERIALS**

www.afm-journal.de

Table 1. Summary of threshold and characteristic temperature of various perovskites.

Materials	Threshold [$\mu J\ cm^{-2}$]	Characteristic Temperature [K]
$CsPb_2Br_5$ microplates[53]	243 (Room temperature)	403
$CsPbBr_3$ nanocuboid[54]	374 (Room temperature)	305
$Cs_{0.1}(MA_{0.17}FA_{0.83})_{0.9}Pb_{0.84}(I_{0.84}Br_{0.16})_{2.68}$[55]	93.53 (Room temperature)	46
$(BA)_2(MA)_{n-1}Pb_nI_{3n}$[35]	13 (140 K)	20
This work	5.6 (Room temperature)	134

in Figure 5a, the temperature-dependent lasing threshold can be well fitted by an exponential function,

$$P_{th}(T) = P_{th,0}\exp\left(\frac{T}{T_c}\right) \tag{8}$$

where T_c is the characteristic temperature related to the gain medium itself and is regarded as an important parameter to evaluate the thermal stability of laser devices. $P_{th,0}$ is the threshold when T approaches zero. It can also be seen from this formula that a high T_c value gives rise to good threshold stability with temperatures. Within temperatures from 60 to 270 K, the ASE threshold changes from 1.02 to 5.11 $\mu J\ cm^{-2}$ (Figure S11, Supporting Information). Based on these results, the value T_c can be fitted as 134 K. It is known that the increase of the pumping threshold of semiconductor materials at elevated temperatures is due to the existence of nonradiative recombination.[51] Therefore, the high value of T_c indicates smaller nonradiative recombination losses. **Table 1** shows the ASE threshold and the characteristic temperature of different reported perovskite samples. Obviously, the sample in this work shows the lowest ASE threshold with a higher characteristic temperature, demonstrating an excellent performance.

Figure 5b shows the long-term stability of laser-treated $CsPbBr_3$ thin film under excitation of 355 nm ns laser pulses (repetition rate 20 Hz, excitation density 80 $\mu J\ cm^{-2}$). The peak position and intensity of ASE are stable during the excitation (as shown in Figure S12, Supporting Information), which maintains for 35 h at room temperature. Even as the temperature increases to 40 °C, the ASE intensity can maintain for at least 12 h. Figure 5c,d shows the scanning electron microscopy (SEM) images of the as-grown and the laser-treated $CsPbBr_3$ thin films, respectively. The as-grown sample shows large-scale agglomeration which may be due to the loss of surface ligands.[52] In comparison, the laser-treated one shows a relatively smooth and dense morphology, which indicates the secondary crystallization. The phenomenon of laser-induced secondary crystallization is useful for applications such as high-capacity graphic coding. This process is similar to image transfer through photolithography. After illumination by 355 nm ns laser, the pattern on the mask can be transferred onto the perovskite thin film. It is worth noting that when excitation density is beyond the threshold, the patterned area shows a bright green ASE as shown in Figure 5e. The use of two intensity levels (SE and ASE, respectively) provides two unique codes. Due to the high flexibility of laser processing, positions in 2D space can also be used as a new sort of information. When multiple locations and intensities are used at the

same time, the number of codes grows exponentially. A five-by-five square matrix has a theoretical coding capacity of about three million. Therefore, laser-induced secondary crystallization offers possibilities for application in optical graphic coding by scanning the emission intensity.

3. Conclusion

In summary, we have demonstrated an advantageous post-treatment for $CsPbBr_3$ NCs thin film by direct laser irradiation. Laser-induced secondary crystallization has been observed during this process, which results in an increase of crystal grain size and improved crystal quality. Optical gain phenomenon has been observed in the laser-treated films. The samples show ASE with a low threshold (5.6 $\mu J\ cm^{-2}$), which is attributed to the effective reduction of nonradiative recombination due to the decreased trap state density, reduced Auger recombination, and weaker exciton–phonon interaction. The exciton–exciton inelastic scattering is considered to be the mechanism of ASE in the laser-treated sample. Furthermore, the laser-treated films exhibit high characteristic temperature and excellent ASE stability. These findings provide a convenient method for perovskite thin film as optical gain medium, which is helpful for understanding the physical mechanisms behind stimulated emission of $CsPbBr_3$ NCs and their application in optoelectronics.

4. Experimental Section

Preparation of Cs-Oleate: Cs_2CO_3 (0.8 g, Aldrich, 99.9%), octadecene (30 mL, Sigma–Aldrich, 90%), and oleic acid (2.5 mL, OA, Sigma–Aldrich, 90%) were added into a 100 mL 3-neck f ask, dried for 1 h at 120 °C, and then heated under N_2 atmosphere to 150 °C until all Cs_2CO_3 reacted with OA. The Cs-oleate had to be pre-heated to 100 °C before injection.

Synthesis of $CsPbBr_3$ NCs: ODE (5 mL) and $PbBr_2$ (0.069 g, ABCR, 98%) were loaded into 25 mL 3-neck f ask and dried under vacuum for 1 h at 120 °C, then added the dried oleylamine (0.5 mL, OLA, Acros 80–90%) and dried OA (0.5 mL) at 120 °C under N_2. After complete solubilization of a $PbBr_2$ salt, the temperature was raised to 140–200 °C (for tuning the NC size) and Cs-oleate solution (0.4 mL, 0.1 m in ODE, 100 °C) was quickly injected, waited for 5 s, cooled the reaction mixture by the ice water bath.

Isolation and purification of $CsPbBr_3$ NCs. The crude solution was cooled down with water bath and aggregated NCs were separated by centrifuging. The tert-butanol (tBuOH, Merck, 99%) was added to the crude solution (ODE:tBuOH = 1:1 by volume) to help complete precipitation. After centrifugation, the supernatant was poured away and the particles were redispersed in hexane.

Structure Characterization: The samples for TEM measurements were prepared by dropping colloidal $CsPbBr_3$ solution with a relatively dilute concentration on carbon-coated 200 mesh copper grids. For the laser-treated TEM samples, the solution had dropped on the copper grids which had been fixed to a quartz plate, then exposed to the nanosecond laser beam for 30 mins. The conventional TEM images were recorded by a Talos F200X microscope equipped with a thermionic gun under an acceleration voltage of 200 kV was used to observe the size and shape of the $CsPbBr_3$ nanocrystals. The SEM (Tescan Mira3) was used to measure the microstructure of the $CsPbBr_3$ films. The absorption spectra were recorded on a UV–vis spectrophotometer (Lambda 950, PerkinElmer, Inc.). The crystal structure of the samples was characterized by XRD on a Rigaku Smartlab XRD System. The FTIR spectra were recorded by a tri-range MIR/NIR/FIR Spectrometer (Spectrum 3, PerkinElmer, Inc.).

Optical Characterizations: Steady-state PL spectra were all recorded by a Shamrock spectrometer (Andor SR-750) and detected by a Newton CCD (model no. DU920P-BU). The 355 nm femtosecond pulse was transformed through an Astrella ultrafast Ti sapphire amplifier (Coherent, 800 nm, 1 kHz, 100 fs) by an ultrafast optical parametric amplifier (Coherent OperA Solo) to perform the power-dependent PL measurement for the evolution of the defect density and the ASE threshold. A variable neutral density filter was used to obtain different excitation powers. In the VSL measurement, the 355 nm femtosecond excitation beam was focused to be a strip line by a cylindrical lens (focus length $f = 75$ mm), the stripe length was controlled by an adjustable slit. For temperature-dependent PL measurements, the sample films were placed into a closed cycle helium cryostat (Cryo Industries of America) with quartz windows, and the temperature was controlled by a commercial temperature controller (Lakeshore 336) from 50 to 295 K. A He-Cd CW laser with a wavelength of 325 nm as the excitation source was used to perform temperature-dependent PL. The 355 nm femtosecond pulsed laser was used as the excitation source to study the temperature-dependent ASE properties and the characteristic temperature. For the ASE stability test, the samples were placed in a heating element that can be kept at a constant temperature, the temperature was maintained at RT (23 °C) and 40 °C. The ASE of the samples was measured every half hour and a 355 nm nanosecond pulse laser (CryLas FTSS355-300-STA) at 20 Hz repetition rate and 1 ns pulse width was used as the excitation source. The TA was measured by the ExciPro femtosecond TA pump-probe spectrometer (CDP Systems Corp.), using the 355 nm femtosecond laser mentioned before as the excitation source.

Supporting Information

Supporting Information is available from the Wiley Online Library or from the author.

Conflict of Interest

The authors declare no conflict of interest.

Data Availability Statement

The data that support the findings of this study are available from the corresponding author upon reasonable request.

[1] C. Wehrenfennig, G. E. Eperon, M. B. Johnston, H. J. Snaith, L. M. Herz, C. Wehrenfennig, G. E. Eperon, M. B. Johnston, H. J. Snaith, L. M. Herz, *Adv. Mater.* **2014**, *26*, 1584.

[2] M. A. Green, A. Ho-Baillie, H. J. Snaith, *Nat. Photonics* **2014**, *8*, 506.

[3] K. X. Steirer, P. Schulz, G. Teeter, V. Stevanovic, M. Yang, K. Zhu, J. J. Berry, *ACS Energy Lett.* **2016**, *1*, 360.

[4] H. Huang, M. I. Bodnarchuk, S. v. Kershaw, M. v. Kovalenko, A. L. Rogach, *ACS Energy Lett.* **2017**, *2*, 2071.

[5] Q. A. Akkerman, G. Rainò, M. V. Kovalenko, L. Manna, *Nat. Mater.* **2018**, *17*, 394.

[6] F. Yan, H. V. Demir, *Nanoscale* **2019**, *11*, 11402.

[7] S. A. Veldhuis, P. P. Boix, N. Yantara, M. Li, T. C. Sum, N. Mathews, S. G. Mhaisalkar, *Adv. Mater.* **2016**, *28*, 6804.

[8] Y. Liang, Q. Shang, M. Li, S. Zhang, X. Liu, Q. Zhang, Y. Liang, Q. Shang, M. Li, Q. Zhang, S. Zhang, X. Liu, *Adv. Funct. Mater.* **2021**, *31*, 2106108.

[9] J. Huang, Y. Shao, Q. Dong, *J. Phys. Chem. Lett.* **2015**, *6*, 3218.

[10] W. A. Dunlap-Shohl, Y. Zhou, N. P. Padture, D. B. Mitzi, *Chem. Rev.* **2018**, *119*, 3193.

[11] Q. Zhou, Z. Jin, H. Li, J. Wang, *Sci. Rep.* **2016**, *6*, 21257.

[12] Z. Wang, X. Liu, Y. Lin, Y. Liao, Q. Wei, H. Chen, J. Qiu, Y. Chen, Y. Zheng, *J. Mater. Chem. A* **2019**, *7*, 2773.

[13] Z. Xiao, Q. Dong, C. Bi, Y. Shao, Y. Yuan, J. Huang, *Adv. Mater.* **2014**, *26*, 6503.

[14] F. Wang, W. Geng, Y. Zhou, H. H. Fang, C. J. Tong, M. A. Loi, L. M. Liu, N. Zhao, *Adv. Mater.* **2016**, *28*, 9986.

[15] F. X. Xie, D. Zhang, H. Su, X. Ren, K. S. Wong, M. Grätzel, W. C. H. Choy, *ACS Nano* **2015**, *9*, 639.

[16] C. Chen, L. Zeng, Z. Jiang, Z. Xu, Y. Chen, Z. Wang, S. Chen, B. Xu, Y. Mai, F. Guo, *Adv. Funct. Mater.* **2022**, *32*, 2107644.

[17] R. Li, B. Li, X. Fang, D. Wang, Y. Shi, X. Liu, R. Chen, Z. Wei, *Adv. Mater.* **2021**, *33*, 2100466.

[18] J. Xue, R. Wang, K. L. Wang, Z. K. Wang, I. Yavuz, Y. Wang, Y. Yang, X. Gao, T. Huang, S. Nuryyeva, J. W. Lee, Y. Duan, L. S. Liao, R. Kaner, Y. Yang, *J. Am. Chem. Soc.* **2019**, *141*, 13948.

[19] T. Udayabhaskararao, M. Kazes, L. Houben, H. Lin, D. Oron, *Chem. Mater.* **2017**, *29*, 1302.

[20] W. Zhihai, W. Jiao, S. Yanni, W. Jun, H. Yafei, W. Pan, W. Nengping, Z. Zhenfu, *J. Mater. Sci.* **2019**, *54*, 6917.

[21] J. Liu, K. Song, Y. Shin, X. Liu, J. Chen, K. X. Yao, J. Pan, C. Yang, J. Yin, L. J. Xu, H. Yang, A. M. El-Zohry, B. Xin, S. Mitra, M. N. Hedhili, I. S. Roqan, O. F. Mohammed, Y. Han, O. M. Bakr, *Chem. Mater.* **2019**, *31*, 6642.

[22] Y. Dong, H. Hu, X. Xu, Y. Gu, C. C. Chueh, B. Cai, D. Yu, Y. Shen, Y. Zou, H. Zeng, *J. Phys. Chem. Lett.* **2019**, *10*, 4149.

[23] J. You, Z. Hong, T. bin Song, L. Meng, Y. Liu, C. Jiang, H. Zhou, W. H. Chang, G. Li, Y. Yang, *Appl. Phys. Lett.* **2014**, *105*, 183902.

[24] S. Huang, Z. Li, B. Wang, N. Zhu, C. Zhang, L. Kong, Q. Zhang, A. Shan, L. Li, *ACS Appl. Mater. Interfaces* **2017**, 9, 7249.

[25] S. K. Sundaram, E. Mazur, *Nat. Mater.* **2002**, 1, 217.

[26] M. J. H. Tan, Y. Chan, *Adv. Mater. Technol.* **2020**, 5, 2000104.

[27] Q. Shang, R. Su, T. T. H. Do, Q. Xiong, *Nano Lett.* **2021**, 21, 1903.

[28] Q. Xiong, S. Huang, J. Du, X. Tang, F. Zeng, Z. Liu, Z. Zhang, T. Shi, J. Yang, D. Wu, H. Lin, Z. Luo, Y. Leng, *Adv. Opt. Mater.* **2020**, 8, 2000977.

[29] J. Yao, J. Zhang, L. Wang, K. Wang, X. Ru, J. Yang, J. Wang, X. Chen, Y. Song, Y. Yin, Y. Lan, Q. Zhang, H. Yao, *J. Phys. Chem. Lett.* **2020**, 11, 9371.

[30] Y. Li, X. Luo, T. Ding, X. Lu, K. Wu, *Angew. Chem. Int. Ed.* **2020**, 59, 14292.

[31] J. Byun, H. Cho, C. Wolf, M. Jang, A. Sadhanala, R. H. Friend, H. Yang, T. W. Lee, *Adv. Mater.* **2016**, 28, 7515.

[32] R. Li, S. Yerci, S. O. Kucheyev, T. van Buuren, L. Dal Negro, S. Yerci, R. Li, S. N. Basu, S. Kucheyev, A. van Buuren, L. Dal, *Opt. Express* **2011**, 19, 5379.

[33] G. Xing, B. Wu, X. Wu, M. Li, B. Du, Q. Wei, J. Guo, E. K. L. Yeow, T. C. Sum, W. Huang, *Nat. Commun.* **2017**, 8, 14558.

[34] Y. Li, X. Luo, T. Ding, X. Lu, K. Wu, *Angew. Chem. Int. Ed.* **2020**, 132, 14398.

[35] Y. Liang, Q. Shang, Q. Wei, L. Zhao, Z. Liu, J. Shi, Y. Zhong, J. Chen, Y. Gao, M. Li, X. Liu, G. Xing, Q. Zhang, P. Y. Microlasers Liang, Q. Shang, Q. Wei, L. Zhao, Z. Liu, Y. Gao, M. Li, Q. Zhang, J. Shi, Y. Zhong, J. Chen, X. Liu, G. Xing, *Adv. Mater.* **2019**, 31, 1903030.

[36] C. M. Iaru, A. Brodu, N. J. J. van Hoof, S. E. T. ter Huurne, J. Buhot, F. Montanarella, S. Buhbut, P. C. M. Christianen, D. Vanmaekelbergh, C. de Mello Donega, J. G. Rivas, P. M. Koenraad, A. Y. Silov, *Nat. Commun.* **2021**, 12, 5844.

[37] A. D. Wright, C. Verdi, R. L. Milot, G. E. Eperon, M. A. Pérez-Osorio, H. J. Snaith, F. Giustino, M. B. Johnston, L. M. Herz, *Nat. Commun.* **2016**, 7, 11755.

[38] A. Shinde, R. Gahlaut, S. Mahamuni, *J. Phys. Chem. C* **2017**, 121, 14872.

[39] Y. Kajino, S. Otake, T. Yamada, K. Kojima, T. Nakamura, A. Wakamiya, Y. Kanemitsu, Y. Yamada, *Phys. Rev. Mater.* **2022**, 6, L043001.

[40] S. C. Boehme, S. ten Brinck, J. Maes, N. Yazdani, F. Zapata, K. Chen, V. Wood, J. M. Hodgkiss, Z. Hens, P. Geiregat, I. Infante, *Nano Lett.* **2020**, 20, 1819.

[41] M. Achermann, A. P. Bartko, J. A. Hollingsworth, V. I. Klimov, *Nat. Phys.* **2006**, 2, 557.

[42] X. Gong, O. Voznyy, A. Jain, W. Liu, R. Sabatini, Z. Piontkowski, G. Walters, G. Bappi, S. Nokhrin, O. Bushuyev, M. Yuan, R. Comin, D. McCamant, S. O. Kelley, E. H. Sargent, *Nat. Mater.* **2018**, 17, 550.

[43] C. M. Iaru, A. Brodu, N. J. J. van Hoof, S. E. T. ter Huurne, J. Buhot, F. Montanarella, S. Buhbut, P. C. M. Christianen, D. Vanmaekelbergh, C. de Mello Donega, J. G. Rivas, P. M. Koenraad, A. Y. Silov, *Nat. Commun.* **2021**, 12, 5844.

[44] A. W. Cohn, A. M. Schimpf, C. E. Gunthardt, D. R. Gamelin, *Nano Lett.* **2013**, 13, 1810.

[45] G. Nagamine, J. O. Rocha, L. G. Bonato, A. F. Nogueira, Z. Zaharieva, A. A. R. Watt, C. H. de Brito Cruz, L. A. Padilha, *J. Phys. Chem. Lett.* **2018**, 9, 3478.

[46] X. Huang, L. Chen, C. Zhang, Z. Qin, B. Yu, X. Wang, M. Xiao, *J. Phys. Chem. Lett.* **2020**, 11, 10173.

[47] Y. Liu, J. Wang, L. Zhang, W. Liu, C. Wu, C. Liu, Z. Wu, Z. Wu, L. Xiao, Z. Chen, S. Wang, S. Wang, S. Wang, S. Wang, *Opt. Express* **2019**, 27, 29124.

[48] A. P. Schlaus, M. S. Spencer, K. Miyata, F. Liu, X. Wang, I. Datta, M. Lipson, A. Pan, X. Y. Zhu, *Nat. Commun.* **2019**, 10, 265.

[49] S. Cheng, Q. Chang, Z. Wang, L. Xiao, E. E. M. Chia, H. Sun, S. Cheng, Q. Chang, L. Xiao, E. E. M. Chia, H. Sun, Z. Wang, *Adv. Opt. Mater.* **2021**, 9, 2100564.

[50] B. Ai, C. Liu, Z. Deng, J. Wang, J. Han, X. Zhao, *Phys. Chem. Chem. Phys.* **2017**, 19, 17349.

[51] B. Liu, R. Chen, X. L. Xu, D. H. Li, Y. Y. Zhao, Z. X. Shen, Q. H. Xiong, H. D. Sun, *J. Phys. Chem. C* **2011**, 115, 12826.

[52] K. Xing, S. Cao, X. Yuan, R. Zeng, H. Li, B. Zou, J. Zhao, *Phys. Chem. Chem. Phys.* **2021**, 23, 17113.

[53] C. Wang, J. Yang, J. Du, T. Shi, W. Liu, X. Tang, Y. Leng, Z. Zhang, Z. Liu, Z. Hu, J. Du, J. Yang, Z. Zhang, Z. Zhang, T. Shi, T. Shi, W. Liu, X. Tang, X. Tang, Y. Leng, Y. Leng, Y. Leng, Y. Leng, Y. Leng, *Photonics Res.* **2020**, 8, 399960.

[54] Z. Liu, J. Yang, J. Du, Z. Hu, T. Shi, Z. Zhang, Y. Liu, X. Tang, Y. Leng, R. Li, *ACS Nano* **2018**, 12, 5923.

[55] P. Brenner, O. Bar-On, M. Jakoby, I. Allegro, B. S. Richards, U. W. Paetzold, I. A. Howard, J. Scheuer, U. Lemmer, *Nat. Commun.* **2019**, 10, 988.